The Vertical structure of a Loop Current Eddy

T. Meunier[1], E. Pallás-Sanz[1], M.Tenreiro[1], E. Portela[1], J. Ochoa[1], A. Ruiz-Angulo[2] and S. Cusí[1]

[1]Departamento de Oceanografía, CICESE, carretera Tijuana-Ensenada 3918, Fraccionamiento Zona Playitas, 22860 Ensenada, B.C.

[2]Centro de Ciencias de la Atmósfera, UNAM, Circuito Exterior s/n, Coyoacan, Ciudad Universitaria, 04510 Ciudad de México, CDMX

Key Points:

- The thermohaline and kinematic vertical structure of a recently detached Loop Current Eddy is revealed in details.
- This structure results from conservative advection of Caribbean water below 200 m, and surface fluxes and diapycnal mixing above.
- The Heat and Salt excess carried by the eddy requires important heat fluxes and fresh water input for balance to be reached in the Gulf of Mexico.

Corresponding author: T. Meunier, thomas.meunier@ifremer.fr

Abstract

The vertical structure of a recently detached Loop Current Eddy (LCE) is studied using in-situ data collected with an underwater glider from August to November 2016. Altimetry and Argo data are analysed to discuss the context of the eddy shedding and evolution as well as the origin and transformation of its thermohaline properties. the LCE appeared as a large body of nearly homogeneous water between 50 and 250 m confined between the seasonal and main thermoclines. A temperature anomaly relative to surrounding Gulf's water of up to 9.7 $°C$ was observed within the eddy core. The salinity structure had a double core pattern. The subsurface fresh core had a negative anomaly of 0.27 psu while the deeper saline core's positive anomaly reached 1.22 psu. Both temperature and salinity maxima were stronger than previously reported. The saline core, of Caribbean origin, was well conserved during its journey from the Yucatan Basin to the Loop Current and at least 7 months after eddy detachment. The fresher homogeneous core resulted from surface diabatic transformations including surface heat fluxes and mixing within the top 200 m during the winter preceding eddy detachment. Heat and salt excess carried by the LCE were large and require important negative heat fluxes and positive fresh water input to be balanced. The geostrophic velocity structure had the form of a subsurface intensified vortex ring.

1 Introduction

The Loop Current (LC) is an intense jet transporting warm and saline Caribbean water from the Yucatan Channel to the Florida Strait (*Austin* [1955]; *Leipper* [1970]), meandering far north in the Gulf of Mexico (GoM) and sporadically shedding anticyclonic vortex rings known as Loop Current Eddies (LCEs) (*Ichiye* [1959]; *Vukovich* [1995]; *Leben* [2005]; *Lugo-Fernández and Leben* [2010]).

The latter are very large structures typically ranging from 200 to 350 km in diameter (*Elliott* [1982]; *Biggs et al.* [1996]) transporting anomalously warm and salty Caribbean water across the GoM. This water mass is composed of Subtropical Under Water (SUW) (*Wüst* [1964]; *Hernández-Guerra and Joyce* [2000]) which is formed by subduction in the subtropical and tropical Atlantic and is characterized by its high salinity ranging from 36.6 to 37.1 between 20.4 and 22.2$°C$ (*O'Connor et al.* [2005]). LCE's typical temperature distribution consists of a subsurface core of warm water, resulting in a downward doming of the isotherms toward the eddy centre, while their salinity signature is obvious as a subsurface saline anomaly (*Elliott* [1982]; *Forristall et al.* [1992]; *Rudnick et al.* [2015]).

After detachment, LCEs drift westward through the central and western GoM, interacting with the Gulf's topography and with neighbouring eddies (*Biggs and Müller-Karger* [1994]) as they reach the western part of the basin. There, they finally decay under the effect of the near-slope topography and geostrophic turbulence (*Lipphardt et al.* [2008]) and the large amounts of heat and salt they carry are diffused, dramatically salinizing the GoM and contributing to the characteristics of the Common Gulf Water (CGW).

LCEs are also extremely energetic. Acoustic Doppler Current Profilers (ADCP) transects and surface drifters revealed velocity maxima ranging from 0.8 $m\ s^{-1}$ (*Indest et al.* [1989]; *Glenn and Ebbesmeyer* [1993]) to over 2.5 $m\ s^{-1}$ (*Koch et al.* [1991]; *Guan et al.* [2011]). The intense currents were shown to be confined within a thin subsurface jet-like crown at the eddy's periphery (*Cooper et al.* [1990]; *Forristall et al.* [1992]; *Guan et al.* [2011]).

LCE's have strong impacts on Hurricane formation and evolution (*Shay et al.* [2000]; *Yablonsky and Ginis* [2013]), thunderstorm occurrence in the southern USA (*Molina et al.* [2016]), ecosystems (*Biggs* [1992]; *Domingues et al.* [2016]), deep water oil drilling operations (*Koch et al.* [1991]), and oil spill stirring (*Goni et al.* [2015]). Most of these impacts strongly depend on LCE's vertical distribution of heat and currents.

The observational work of *Elliott* [1982],*Cooper et al.* [1990], and *Forristall et al.* [1992] have provided a valuable description of LCE's thermohaline vertical structure, including the existence of the salinity maximum and the core pycnostat. However, in-situ observations of recently detached LCEs remained rare and often restricted to ADCP, sparse XBT transects or punctual CTD stations (*Indest et al.* [1989]; *Glenn and Ebbesmeyer* [1993]; *Guan et al.* [2011], among many). For the last 2 decades, LCEs were mostly described through altimetry and regional modelling, focusing on their formation process (see for instance *Chang and Oey* [2010a]; *Schmitz* [2005]; *Le HéNaff et al.* [2012]), detachment statistics (*Hamilton et al.* [1999]; *Leben* [2005]; *Lugo-Fernández and Leben* [2010]) or designing forecasting systems (*Oey et al.* [2005]; *Hoteit et al.* [2013]. While these studies greatly increased the understanding of LCE dynamics, detailed in-situ observations of LCE's vertical structure remain necessary to validate numerical models configurations, and fully understand LCE's life cycle and contribution to the GoM's dynamics.

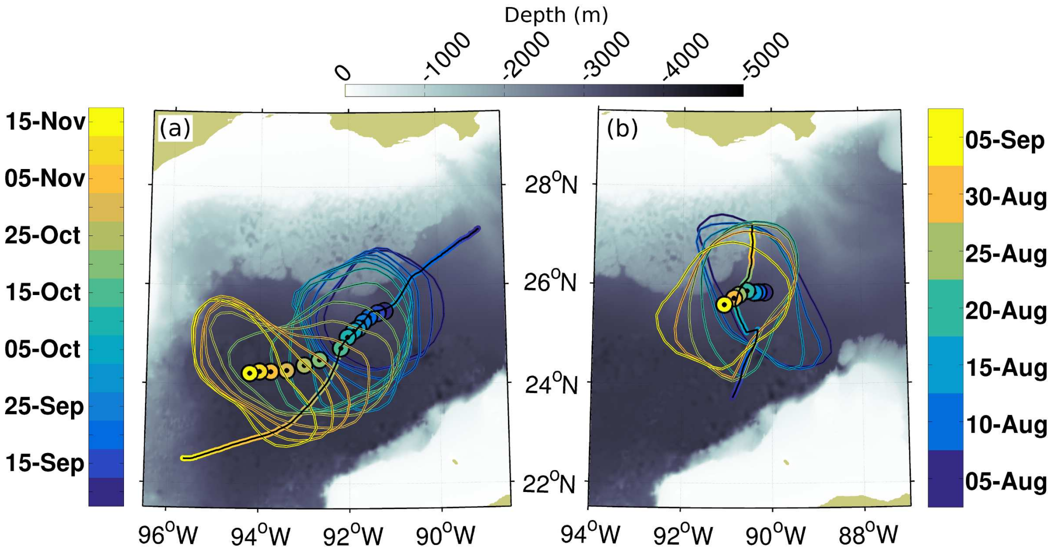

Figure 1. Glider track and eddy position during section 1 (panel b) and 2 (panel a). The closed contours are the 0.7 m ADT isopleth. The glider track is materialized by the continuous thick line. Dots were plotted at the estimated eddy centre. Time is colour-coded for each section to help the interpretation. Bathymetry of the Gulf of Mexico is represented by the grey scale map.

The advent of Underwater Gliders over the last 15 years brought a flexible and cost-reduced alternative to ship surveys (*Eriksen et al.* [2001]; *Rudnick et al.* [2004]) and they were shown to be suited to sample mesoscale structures such as coastal currents, eddies and fronts (*Rudnick et al.* [2004]; *Rudnick et al.* [2015]; *Ruiz et al.* [2009]; *Pietri et al.* [2014], among many), including LCEs and frontal cyclones in the GoM as shown by *Rudnick et al.* [2015].

In the purpose of studying LCE's vertical structure, a glider mission was designed and successfully performed in the central GoM. The glider repeatedly crossed the recently detached LCE Poseidon from 05/08/2016 to 15/11/2016. This paper describes in detail its anatomy and evolution, and discusses the possible processes leading to it with the help of complementary altimetry and Argo float data.

2 Data and Methods

2.1 Glider and sampling Strategy

The data were collected using a *Kongsberg Seaglider*^{TM} autonomous underwater vehicle in the central GoM, totalizing 625 dive cycles from 05/08/2016 to 15/11/2016. The glider navigated up and down from the surface down to 1000 dBar at an average horizontal speed of 0.15 $m\ s^{-1}$ in the Earth referential and average vertical speed of 0.15 $m\ s^{-1}$. On average, the distance between two consecutive surfacing events was of 2 km, but was quite variable, with a standard deviation of 870 m and extrema of 500 m and 6.5 km.

The mission was designed to cross LCE Poseidon through its centre and as parallel as possible to the thermohaline gradients. This has been proven to be a difficult exercise because of the relative slowness of the glider compared to the intense near-surface currents at the periphery of LCEs (*Rudnick et al.* [2015]). To manage this challenging task, the piloting strategy included adapting the glider's buoyancy to increase its horizontal speed when facing strong currents, which in turn also increased its vertical speed, minimizing the time spent within these near-surface currents.

AVISO Absolute Dynamic Topography (ADT) gridded 10-days composites, produced and distributed by CNES (http://www.aviso.altimetry.fr/en/my-aviso.html), were used as a proxy for the thermohaline structure of the eddy to determine the optimum along gradient trajectory. The glider's heading was automatically corrected in near real time (before each new dive) using a hydrodynamical flight model and drift data from previous dives.

Figure 1 shows the glider's track superimposed on the 0.7 m isopleth of ADT associated with Poseidon during both transects. Dots represent the successive eddy centre positions computed as the centroid of these ADT isopleths. In both cases, the glider crossed the eddy from end-to-end, closely approaching its centre, and following a reasonably straight path despite the rapid evolution of the ADT situation and the strong currents. The interruption of section 1 around 15/08 is a notable exception: The fast rotation of the elliptic eddy's major axis forced a quick repositioning of the glider to recover an along-gradient trajectory.

2.2 Mounted instruments and data correction

The glider was equipped with an unpumped *Seabird CT Sail* CTD probe with a sampling rate of 0.15 Hz, ensuring a mean vertical resolution of 2 m. Unpumped CTDs are well known to suffer from increased discrepancies of the measured conductivity in zones of rapidly varying temperature. This issue, known as Thermal lag (*Lueck* [1990]; *Lueck and Picklo* [1990]), resulted in large amplitude and high wave number salinity inversions or 'spiking' in some profiles. The data were therefore corrected using *Garau et al.* [2011]'s algorithm which is designed to supress thermal lag effects for variable sampling rate and flow speed CTDs. The efficiency of the method was tested using data from a previous mission where a pumped CTD was mounted along with the *Seabird CT Sail* CTD (not shown). Residual errors never exceeded 0.03 psu. The correction magnitude was maximum outside the eddy, near the surface, in the seasonal thermocline, where it eventually reached 0.25 psu. Below the eddy, near its outer edge where the main thermocline is sharp, significant correction (upto 0.06 psu) was also applied by the method.

The corrected data were interpolated on a regular grid using the Barnes objective analysis scheme (*Barnes* [1964, 1994]). It is an iterative convergent weighted-averaging interpolation scheme commonly used in meteorology and oceanography and proven to be sound. Vertical and horizontal decorrelation scales of respectively 20 m and 30 km were chosen to avoid aliasing effect of internal waves (*Rudnick and Cole* [2011]) without loosing too much details. Vertical and horizontal grid steps of respectively 2 m and 2 km were chosen to fit the original glider data resolution.

Absolute geostrophic velocity was computed using the thermal wind relations and the top 1000 dBar averaged velocity inferred from the Glider's drift as the reference velocity, following *Rudnick et al.* [2015]:

$$u_g(r,z) = \overline{U} + \frac{g}{\rho_0 f H}\iint_{-H}^{0} \partial_r \rho dz^2 - \frac{g}{\rho_0 f}\int_{-H}^{0} \partial_r \rho dz, \qquad (1)$$

where $u_g(r,z)$ is the absolute geostrophic velocity, g is the gravity acceleration, f is the coriolis frequency, H is the deepest sampled depth (1000 m here), $\overline{U}$ is the velocity averaged over the depth H inferred from the glider's drift between two consecutive surfacing, ρ is the density as measured by the glider, and r is the curvilinear coordinate following the glider's trajectory. A discussion on the error associated with lack of synopticity can be found in section 4.

2.3 Argo float data

Argo profiling float data were used to describe the hydrographic context in the Yucatan basin and the LC prior to the glider mission, to validate the glider data and to determine average GoM temperature, salinity and potential density vertical profiles $[\overline{T},\overline{S},\overline{\sigma}](z)$. The main purpose of computing a mean state GoM profile is to asses the thermohaline anomalies associated with Poseidon, relative to the surrounding water at the time of the survey. It is therefore not to be thought of as a climatological definition of the typical GoM water, as the latter may experience seasonal and interannual variability. A number of selection criteria were applied to the ARGO data base to compute this base state profile: the profiles were selected to be well outside Poseidon or any remnant of previously detached LCEs, using the 0.5 m ADT isopleth as a reference. Profiles from the northern shelf and slope were excluded to avoid contamination of the mean profile by Missisipi river plume water. 39 profiles were found to meet these criteria between 01 April and 01 November 2016. A list of the profile references, dates and positions is shown in table A: . Their positions are shown in the ADT maps of figure 2.

Anomalies were computed as follow:

$$[T',S',\sigma'](x,y,z,t) = [T,S,\sigma](x,y,z,t) - [\overline{T},\overline{S},\overline{\sigma}](z), \tag{2}$$

where $[T,S,\sigma](x,y,z,t)$ are temperature, salinity and potential density measured by the glider.

Mixed layer depth was computed from Argo float profiles and Glider data following *Thomson and Fine* [2003]. The method consists in finding the deepest data point of the water column which potential density varies by less than 0.03 $kg\ m^{-3}$ from a reference depth of 5 m. Following the same approach, we defined a homogeneous salinity layer satisfying a similar criterion with a threshold value of 0.03 psu.

2.4 Heat and salt contents

The eddy's total heat and salt contents were computed following *Elliott* [1982] and *Armi et al.* [1989]. Assuming conservation of volume (the same volume of GoM water exits as LCE water enters) and axisymmetry of the eddy, the extra heat and salt carried by Poseidon reads :

$$\hat{Q} = \int_{-\pi}^{\pi} \int_{0}^{P_b} \int_{0}^{R} C_p T' r dr \frac{dP}{g} d\theta, \tag{3}$$
$$\hat{S} = \int_{-\pi}^{\pi} \int_{0}^{P_b} \int_{0}^{R} \frac{S'}{1000} r dr \frac{dP}{g} d\theta, \tag{4}$$

where P_b is the pressure (in Pa) at the bottom of the eddy (1000 dBar = $\times$ 10^7 Pa), R is the radius of the eddy, C_p is the specific heat capacity, g is the gravity acceleration, T' is the temperature anomaly as defined in equation 2 and S' is the salinity anomaly using the approximation that 1 psu is equivalent to 1 $g\ kg^{-1}$.

The slowness of the glider and the rapid drift of the eddy may result in an over-estimation of the eddy radius when both move in the same direction, and an under-estimation when they move in opposite directions. The radius used to integrate the heat and salt anomaly thus requires correction. The eventual eddy deformation into an elliptical or irregular shape also encourages this correction. A reference eddy area $\mathcal{A}_{06}$ defined as the surface enclosed within the 0.6 m ADT isopleth was used for correction. Using the approximation that the eddy radius does not depend on pressure, the corrected heat and salt contents are defined as :

$$\hat{Q}_c = \frac{\mathcal{A}_{06}}{\pi R^2} \hat{Q} \tag{5}$$
$$\hat{S}_c = \frac{\mathcal{A}_{06}}{\pi R^2} \hat{S}. \tag{6}$$

3 Results

3.1 Context

3.1.1 Altimetry

A sequence of ADT snapshots from 01 April to 01 November is shown in figure 2. Red dots represent the eddy centre defined as the centroid of the 0.7 m ADT isopleth. Its drift speed and heading are plotted against longitude in figure 3a. The evolution of the ADT maximum, and of the eddy's surface defined as the area enclosed within the 0.6 m ADT isopleth are shown in figure 3b.

After a series of necking downs, detachments and reattachments starting in July 2015 (not shown), a large meander of the LC ultimately pinched-off in early April under the joint effect of two frontal cyclones: one near the West-Florida shelf and the other east

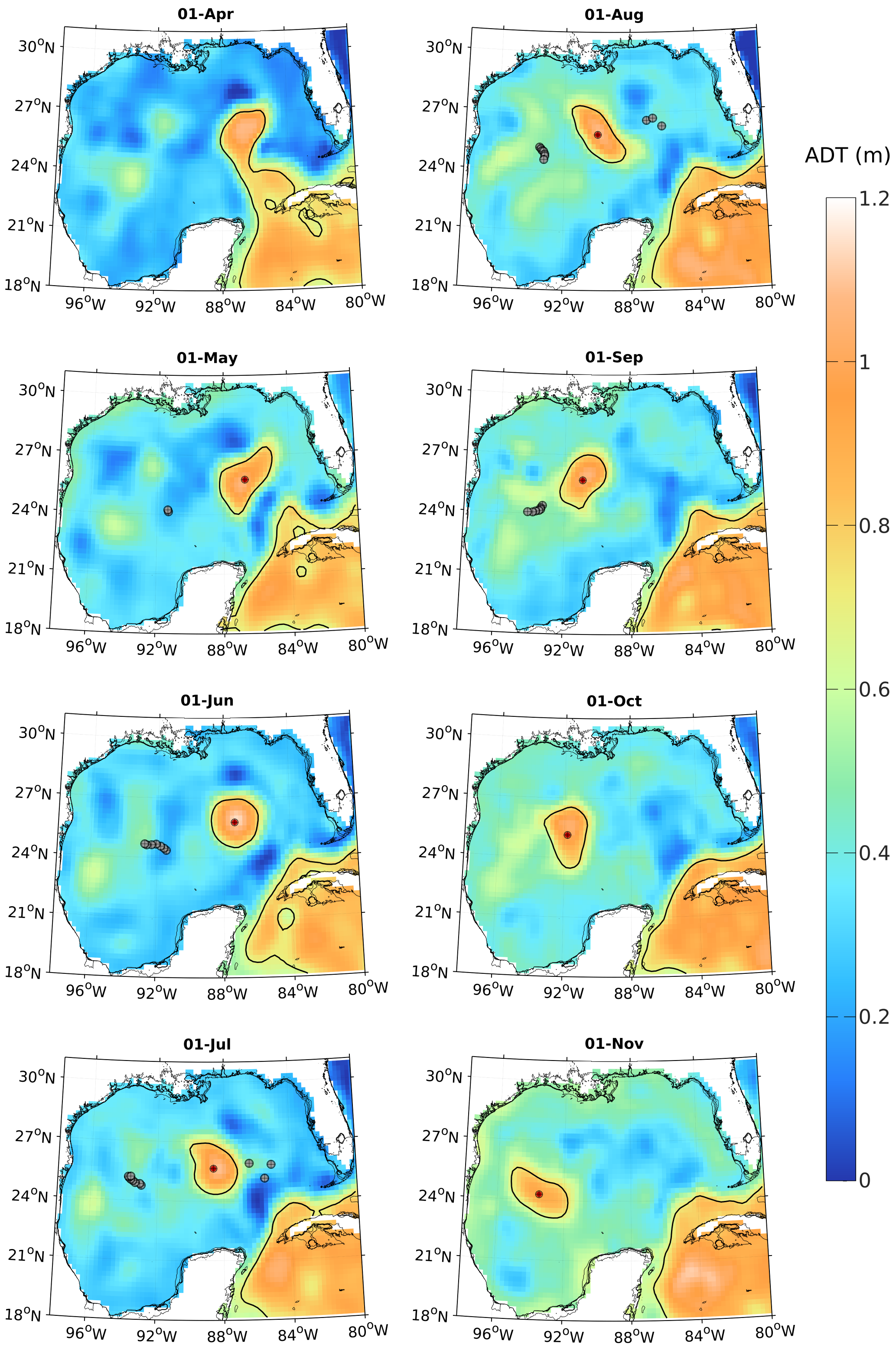

Figure 2. Snapshots of Absolute Dynamic Topography (m) from 01 April to 01 November 2016. The 0.7 m ADT isopleth is materialized by a black contour line. The red dots stand for the centroid of the 0.7 m ADT isopleth. The grey dots represent the location of the Argo profiles available during this time lapse. A list of the latter is available in table A: .

of the Campeche bank. It resulted in the shedding of the large and elliptic LCE Poseidon on 15 April, while the two small frontal eddies merged into a large cyclonic anomaly extending from the Campeche Bank to the West Florida shelf. Poseidon was characterized by an ADT maximum of 1.15 m. Along its major axis, its diameter reached respectively 300 and 350 km considering the 0.7 and 0.6 m ADT isopleths as its outer edge. The area enclosed within the latter ADT isopleths was of 6.7×10^4 and 8.7×10^4 km^2, respectively. In early June, Poseidon axisymmetrized into a circular structure with a diameter of respectively 290 and 310 km considering the 0.7 and 0.6 m ADT isopleths. It was centred near 87.5°W 25.7°N. In the mean time, the LC position gradually switched into *port to port mode* as the small remaining meander decayed. From May to July, Poseidon slowly drifted westward with a variable speed (between 2 and 7 $cm\ s^{-1}$) and heading (between 230 and 280°) (figure 3a). In July, Poseidon started to distort, evolving into an elliptical eddy again, not without recalling a mode 2 instability in early August at the beginning of the first glider transect. It then re-axisisymmetrized quickly between 10 and 25 August, forcing a repositioning of the glider. During transect 1, the eddy drift speed was highly variable, ranging between 3 and 10 $cm\ s^{-1}$. In September, the eddy shape did not change drastically. Its centre drifted southwestward at the average speed of 4.5 $cm\ s^{-1}$ as the glider started its way through the second transect. From Poseidon's detachment to the end of September, the maximum ADT had only decreased by 10 cm. From early October to early November, the eddy drift speed increased to reach 12 $cm\ s^{-1}$ and the ADT maximum started to drop (figure 3b) as it moved west of 92°W. Both the eddy drift and the ADT maximum erosion then seemed to slow down in November, while Poseidon evolved into an elliptical eddy again until the end of the glider mission on 15/11.

During the first 6 month of its life, Poseidon's ADT maximum decreased in average of 1.2 $mm\ d^{-1}$. The area enclosed within the 0.8 ADT isopleth decreased from 4.7 to 2.8 $\times\ 10^4$ km^2 in 6 months while that enclosed within the 0.6 ADT isopleth only decreased from 6.2×10^4 to 5.9×10^4 km^2, suggesting a subsidence of the ADT anomaly rather than a net erosion.

It's centre drifted from 87 to 94 $°W$ at an average speed of 5.2 $cm\ s^{-1}$ with a standard deviation of 3.5 $cm\ s^{-1}$, heading west/southwest (average heading of 244°). In a generalization of the pioneering work of *Nof* [1981] on the β-drift of interior vortices, *Cushman-Roisin et al.* [1990] proposed a one and a half layer analytical solution for the drift of mesoscale eddies, which reads:

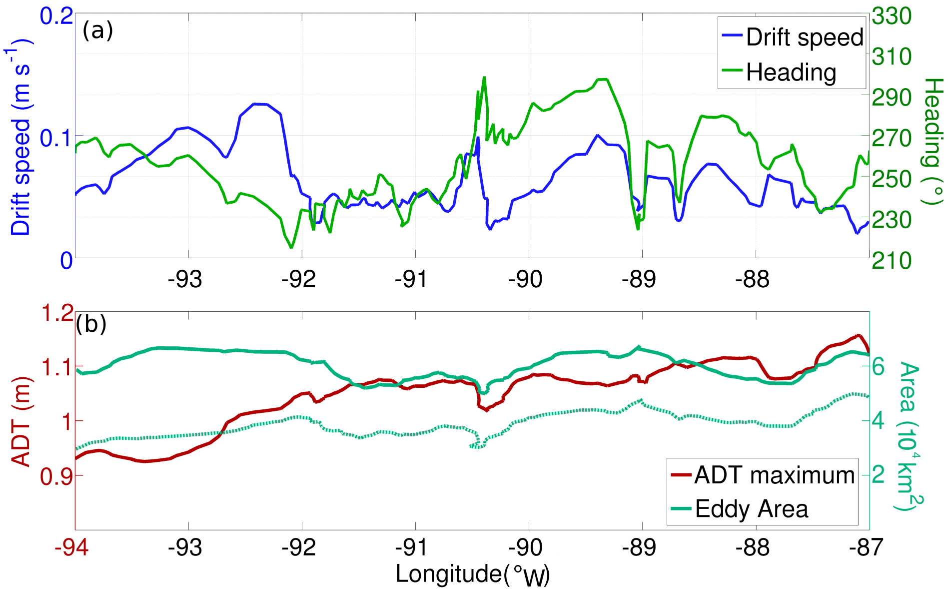

Figure 3. (a): Drift speed in $m\ s^{-1}$ (blue line) and heading in ° (green line) of the eddy centre against longitude (bottom x-axis) and time (top x-axis). (b): Maximum Absolute Dynamic Topography (ADT) value inside the eddy (m) (red line), and area enclosed within the 0.8 and 0.6 m ADT isopleth (dashed and continuous green lines) against longitude (bottom x-axis) and time (top x-axis).

$$U_d = -\frac{\beta_0 g'}{f_0^2}\frac{\iint H\eta + \frac{1}{2}\eta^2 dxdy}{\iint \eta dxdy}, \tag{7}$$

where U_d is the eddy's drift speed, β_0 is the meridional derivative of the Coriolis frequency, g' is the reduced gravity, H is the average thickness of the active layer, and η is the vertical deviation of the interface between the layers. Using Poseidon's characteristics ($\beta_0 = 2 \times 10^{-11}\ s^{-1}\ m{-1}$, $g' = 0.038$, $f0 = 6.4 \times 10^{-5}\ s^{-1}$, $H = 150m$, and the depth of the 1026 $kg\ m{-3}$ as a measure of η), the theoretically expected drift speed is of $3.8 \pm 0.2\ m\ s^{-1}$, 30% smaller than the average observed drift. This faster mean drift, along with a large variability, eventually reaching 3 times the theoretical prediction, suggests a possibly significant impact of topographic effects, or interactions with neighboring mesoscale structures on the westward motion of Poseidon.

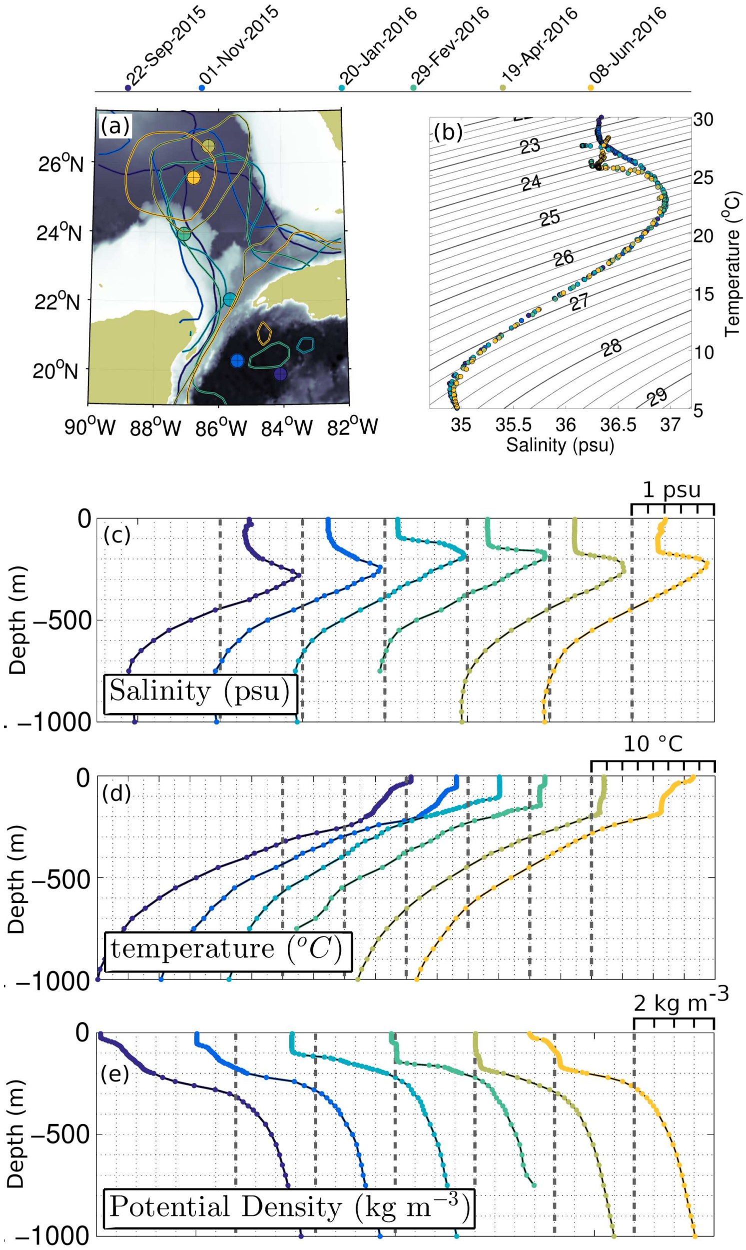

Figure 4. Selected Argo float profiles in the northwest Caribbean, Yucatan channel, Loop Current, and Poseidon. Time is colour-coded. (a): Position of the Argo profiles (coloured dots). The contours are the 0.7 m ADT isopleths. The grey-scale map represents the GoM's bathymetry. (b): T-S diagram of the Argo profiles. (c): Vertical profiles of salinity. The 36 psu reference is materialized as black dotted lines. (d): Vertical profiles of Temperature. The $20^o C$ reference is materialized as black dotted lines. (e): Vertical profiles of Potential density. The 24 $kg\ m^{-3}$ reference is materialized as black dotted lines.

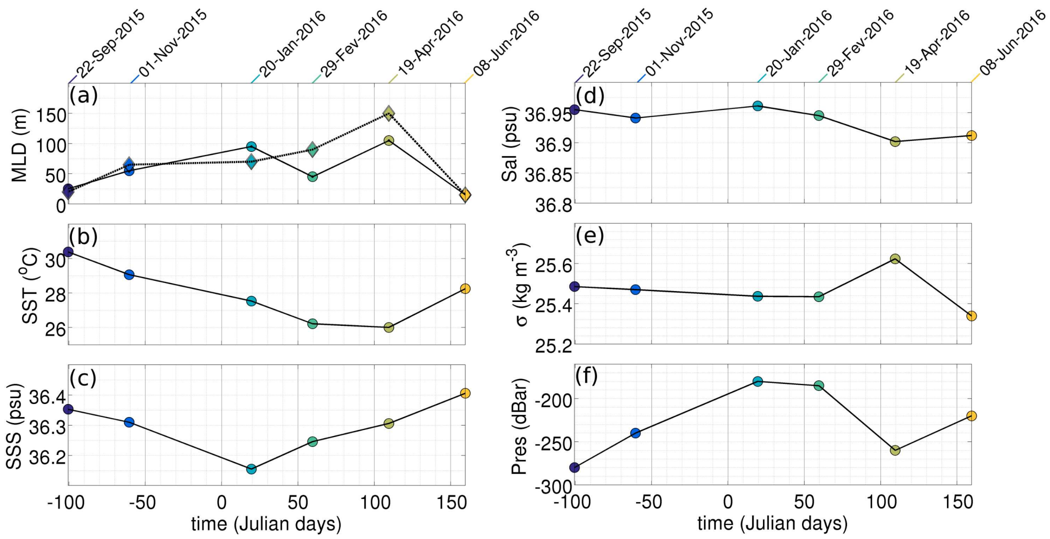

Figure 5. Properties of the sea surface and the salinity maximum for each Argo profiles in the northwest Caribbean, Yucatan channel, Loop Current and Poseidon. The bottom x-axis represents time in days from 01/01/2016. Reference calendar dates are shown in the top x-axis. Time is also colour-coded in the figures. (a):Mixed layer depth. (b): Sea Surface Temperature (SST). (c): Sea Surface Salinity (SSS). (d) Salinity maximum. (e): Potential density at the salinity maximum. (f): Pressure at the salinity maximum.

3.1.2 Preceding hydrographic conditions

Figures 4 and 5 show the water mass evolution measured by the Argo float 4901061 from September 2015 to June 2016 as it drifted from the northwest Caribbean to the tip of the LC.

The salinity maximum (36.95 psu), typical of the Caribbean water was obvious in all profiles from the Yucatan Basin to the very tip of the LC and after the eddy detachment (figures 4c and 5d). It was found between the 25.45 and the 25.50 $kg\ m^{-3}$ isopycnals in the Yucatan Basin through the southwestern edge of the LC, then exhibited more variability as it reached the tip of the LC (figure 5e). The depth of the salinity maximum ranged from 280 to 180 m (figure 5f). The T-S diagram from figure 4b suggests that below the 24.50 $kg\ m^{-3}$ isopycnal, the water mass found from the Caribbean to the tip of the LC and within Poseidon was the same.

On the contrary, large differences in surface and subsurface hydrographic properties are obvious between the Yucatan basin's September situation and that of Poseidon in June. The strong near surface stratification obvious in the temperature, salinity and potential density profiles of the northwest Caribbean (Figure 4c,d,e) resulted in a shallow mixed layer (25 m) (Figure 5a). The mixed layer deepened to reach 105 m on 19 April, when Poseidon detached. The depth of the surface homogeneous salinity layer increased from 20 to 140 m during the same period. The second profile within the recently detached Poseidon (08 June) suggests an increase of surface salinity (Figure 5c) along with an increase of surface temperature (Figure 5b) resulting in a re-stratification associated with a quick decrease of the mixed layer depth. The evolution of the near surface thermohaline properties appears in figure 4b as a divergence of the profiles in the T-S plane above the 24.5 $kg\ m^{-3}$ isopycnal (25.5 $°C$ isotherm), consistent with water mass transformation through surface heat fluxes.

3.2 The Glider survey

3.2.1 Temperature

The eddy is obvious as a large body of homogeneous warm water, between 24.1 and 26.7$°N$, in section 1 and between 23 and 26$°N$ in section 2 (figures 6a and 7a, respectively). It splits the thermocline in half, deviating the warm near-surface isotherms ($> 26^oC$) upward, and the cooler ones ($< 25^oC$) downward. While outside the eddy, the 25 and 27.5 ^oC isotherms are only 10 and 15 m appart in sections 1 and 2, respectively, this distance reaches 190 and 160 m within the eddy core. Below 25 ^oC, all isotherms are doming downward, toward the eddy centre: in section 1 (2), the 20$°C$ isotherm drops from 140 (100) m at the eddy periphery to 350 (295) m near its centre. This temperature distribution results in a lens-like temperature anomaly reaching a maximum of +9.7$°C$ at 230 m in section 1 and +8.7$°C$ at 200 m in section 2 (figures 6b and 7b). The anomaly remains strong in depth in both sections (4$°C$ at 500 m and 2$°C$ at 700 m). In neither of the two sections seems the eddy to affect SST (figure 8b). However, contrary to section 1, a north-south asymmetry appears in the SST distribution of section 2, which drops from 30.5 to 28.5 $°C$ from north to south (Figure 8b).

3.2.2 Salinity

In both sections, the eddy has a striking double core salinity structure: A lens-like homogeneous core of fresher water in subsurface sits right over a deeper saline core (figures 6c,d and 7c,d). The fresh anomaly reaches -0.27 and -0.25 psu in sections 1 and 2,

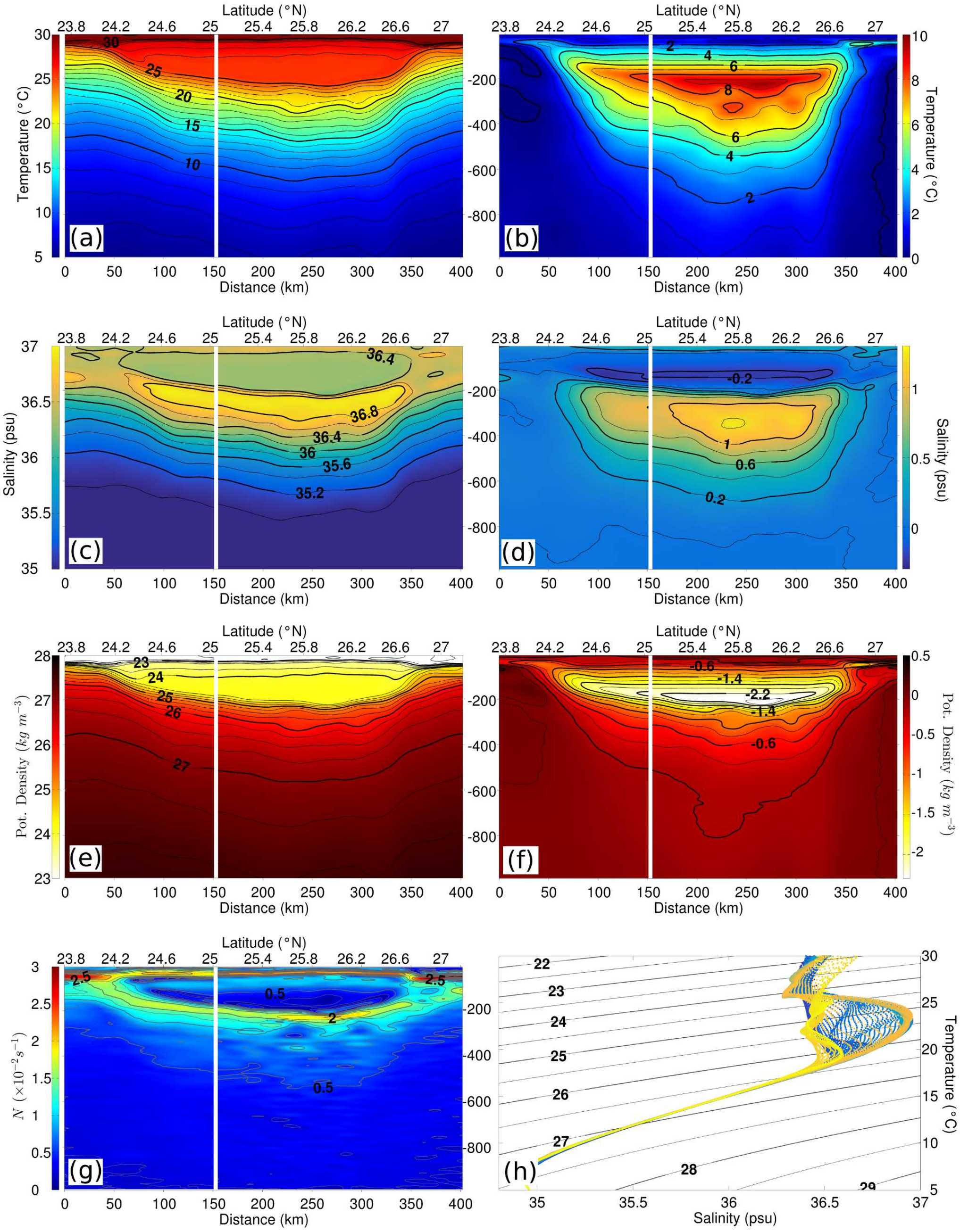

Figure 6. Hydrographic properties along Section 1. The bottom x-axis is the distance from the start of the transect while the top x-axis is the latitude. Vertical sections of (a):Temperature ($^\circ C$), (b): Temperature anomaly ($^\circ C$) as defined in equation 2, (c): Salinity (psu), (d): Salinity anomaly (psu), (e): Potential Density referenced to the surface ($kg\ m^{-3}$), (f): Potential Density anomaly ($kg\ m^{-3}$), (g): Brunt-Väisälä frequency (s^{-1}). (h): T-S diagram of all profiles collected during transect 1. Time is colour-coded as in figure 1.

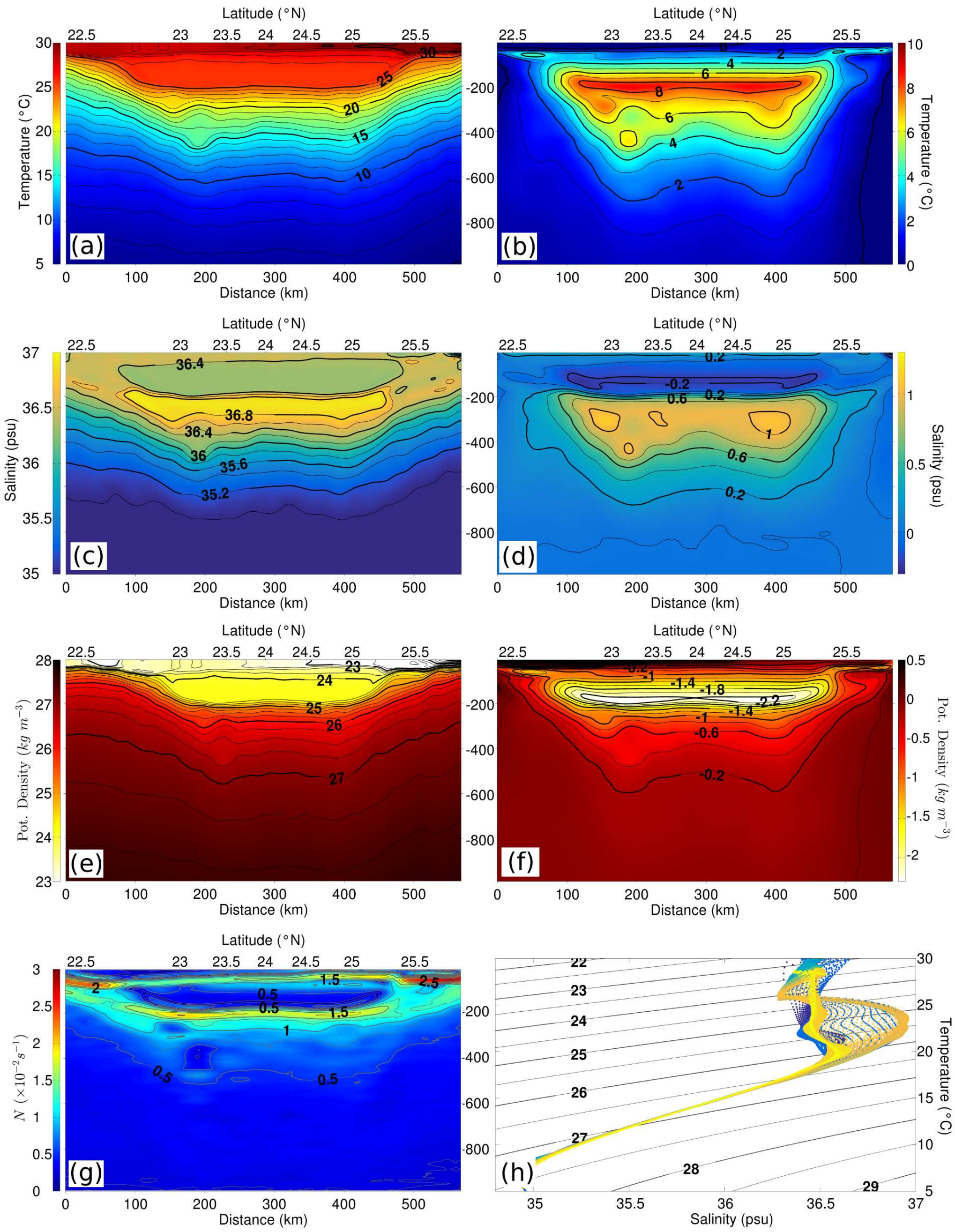

296 **Figure 7.** Same as figure 6 for section 2.

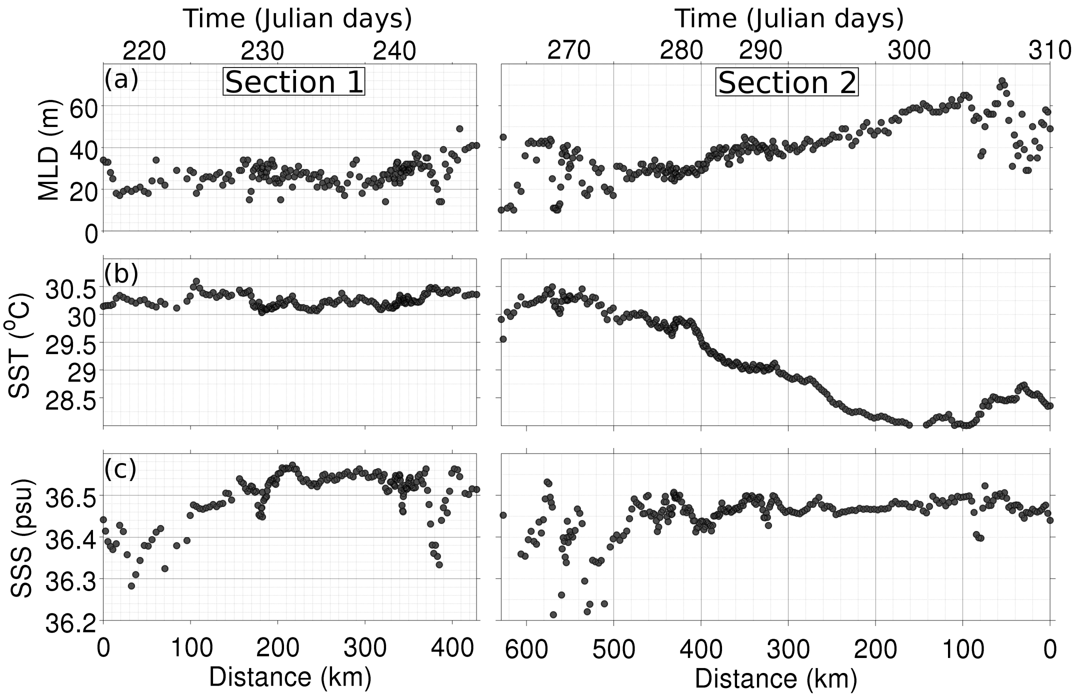

Figure 8. Sea Surface properties along the glider trajectory in section 1 and 2. (a): Mixed Layer Depth (MLD), (b) Sea Surface Temperature (SST), (c): Sea Surface Salinity (SSS). The bottom and top x-axis are distance and time, respectively.

respectively. It is enclosed within the 36.4 psu isohaline, which extends vertically from 30 to 200 m (50 to 180 m) and laterally from 24.2 to 26.6°N (22.7 to 25.4°N) in section 1 (2). Right below, separated from the fresh core by a sharp halocline, the saline core extends from 220 m to 650 m. It is obvious in both sections as a lens-like positive salinity anomaly, reaching +36.97 psu (+1.22 psu anomaly) at about 230 m in the central part of the eddy. Detailed properties of the salinity maximum of each profile are shown in figure 9. In both sections, the eddy is obvious as a steep rise of the local maximum (panel a). The potential density at the salinity maximum (panel b) is centred around 25.45 $kg\ m^{-3}$ within the eddy, consistant with typical SUW, while outside, it is centred around 26 $kg\ m^{-3}$, consistant with CGW. While the salinity maximum is centred on the same potential density level in both sections, the depth of the latter varied significantly between the two sections: it raised from 275 m in section 1 to 240 m in section 2 (panel c).

At the surface, salinity is slightly higher above the eddy and shows less variability than at its periphery (figure 8c).The homogeneous salinity layer is only 20 to 30 m deep in section 1, while it reaches 100 m outside the eddy (figure 6c). In section 2, the north-

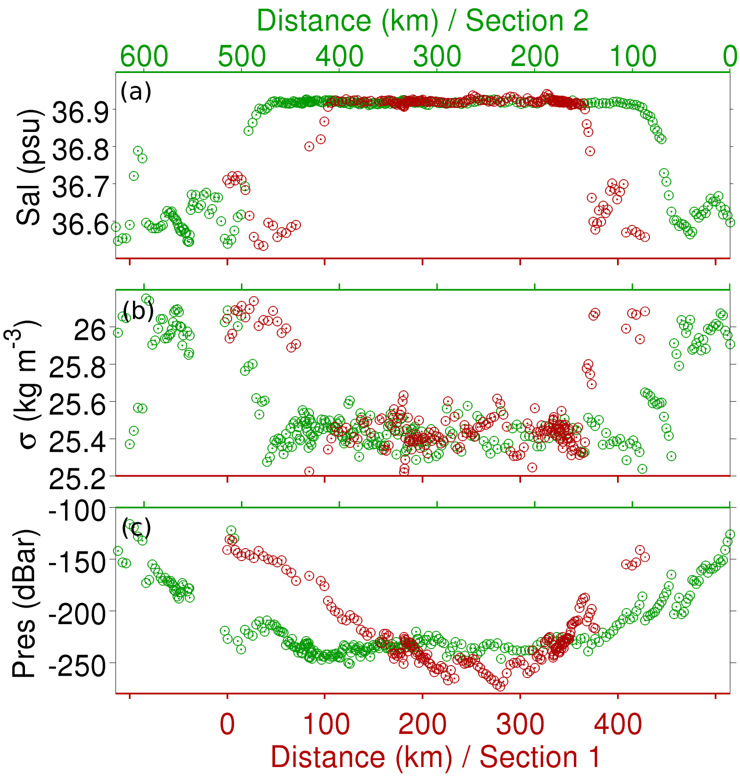

315 **Figure 9.** Properties of the local salinity maximum. (a): Salinity maximum. (b): Potential density at the salinity maximum. (c): Depth of the salinity maximum. Red and green circles stand for sections 1 and 2, respectively.

south asymmetry found in SST is not detectable in SSS but shows in the thickness of the homogeneous salinity surface layer: it is 100 m deep at the southern edge of the section while it is only 70 m deep at the northern edge (figure 7c).

3.2.3 Potential density

The signature of the eddy in terms of potential density closely resembles that of temperature, which dominates over salinity (figures 6e and 7e): In both sections, the eddy core is obvious as a body of homogeneous buoyant water, with a density anomaly reaching $-2.5\ kg\ m^{-3}$ at 220 m in section 1 (figures 6f) and $-2.3\ kg\ m^{-3}$ at 190 m in section 2 (Figure 7f). This density anomaly splits the pycnocline in half as isopycnals are doming upward in subsurface and downward below. Outside the eddy, the 23.5 and 25 isopycnals are separated by about 30 and 35 m while they are 190 and 160 m apart within the eddy core in sections 1 and 2, respectively. The density signature of the eddy has a deep extension, as an anomaly of $0.1\ kg\ m^{-3}$ is still detectable at 1000 m.

The Brunt-Väisälä frequency sections of figures 6g and 7g reveal the intra-pycnocline nature of the eddy: The strong stratification strip ($1.5 \times 10^{-2}\ s^{-1} < N < 2.5 \times 10^{-2}\ s^{-1}$) associated with the pycnocline is split in half into two slightly weaker strips surrounding the eddy core. The latter is obvious as a body of extremely weakly stratified water ($N < 5 \times 10^{-3}\ s^{-1}$).

Near the surface, while the mixed layer depth in section 1 varies little (between 25 and 35 m) and is not afected by the eddy, a striking north-south asymmetry appears in section 2 (figure 8a). The mixed layer considerably deepens from north (30 m) to south (60 m). The upper pycnocline consequently slopes downward toward the south: At $23°N$, the Brunt-Väisälä frequency maximum is centred near 70 m , while in the northern edge of the eddy, it lays near 30 m (figure 7g)

3.2.4 Velocity

Deflection of the isopycnals induces a strong horizontal density gradient on the periphery of the eddy. The resulting geostrophic velocity field shows two well defined peaks around these narrow fronts (figure 10a and c). The velocity structure exhibits notable differences between sections 1 and 2 as well as a clear north-south asymmetry in each section.

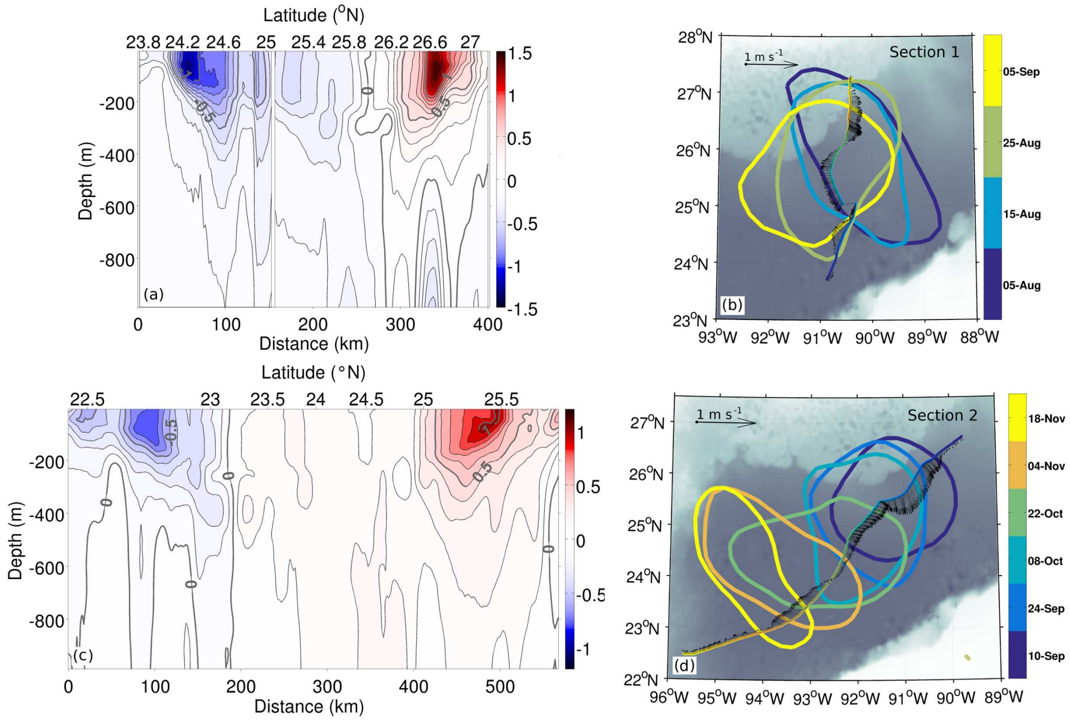

Figure 10. (a): Vertical section of absolute geostrophic velocity ($m\ s^{-1}$) along transect 1 as defined in equation (1). The thick and thin contours are plotted respectively every 0.5 and 0.1 $m\ s^{-1}$. The southern and northern velocity maxima are of 1.10 and 1.55 $m\ s^{-1}$, respectively. (b): Horizontal distribution of the depth averaged velocity inferred from the glider's drift for section 1. The black arrow in the left-hand side corner represents a 1 $m\ s^{-1}$ velocity. The 0.7 m ADT isopleths are represented by the closed contours. (c): Same as (a) for section 2.The southern and northern velocity maxima are of 0.79 and 1.22 $m\ s^{-1}$, respectively. (c): Same as (b) for section 2.

In section 1, the southern velocity maximum reaches 1.1 $m\ s^{-1}$ in subsurface (70 m) at 24.3°N. It lays within a larger core of high velocity that can be defined by the 0.5 $m\ s^{-1}$ isotach extending from 24.1 and 24.7°N and reaching the depth of 320 m. The velocity shear is intense (up to $5 \times 10^{-3}\ s^{-1}$) between 100 and 300 m and currents are weak below 500 m (<0.1 $m\ s^{-1}$). North of the data gap (around 25.2°N), a weaker and more homogeneous velocity maximum of 0.45 $m\ s^{-1}$ extends from the surface down to 200 m. The northern core of high velocity is centred at 26.7°N where it reaches 1.55 $m\ s^{-1}$ at 80 m. It is wider than the southern core: the 0.5 $m\ s^{-1}$ isotach extends between 26.3 and 27.1°N. Below the northern core, there is evidence of a flow reversal at 500 m, intensifying with depth and reaching 0.3 $m\ s^{-1}$ at 1000 m.

In section 2, velocity reaches 0.79 $m\ s^{-1}$ at 80 m in the southern maximum (23.2°N) and 1.22 $m\ s^{-1}$ at 60 m in the northern maximum (25.85°N). The 0.5 $m\ s^{-1}$ isotachs enclose the high velocity cores: in the south, it is 50 km wide and reaches the depth of 180 m while in the north it is 70 km wide and 280 m deep. In the central part of the eddy, between 24 and 25.5°N, a nearly homogeneous current between 0.10 and 0.25 $m\ s^{-1}$ flows in the same direction as the northern velocity maximum.

The direction of the depth averaged current inferred from the glider's drift is shown in figures10b and d. It validates the representativeness of the geostrophic velocity for most of the two transects: the current was well perpendicular to the glider's track as it crossed the southern and northern high velocity cores in both sections. A slightly more along track direction of the velocity in section 1 between 25 and 26°N suggests that the weakness of the secondary velocity maximum encountered north of the data gap may result from the temporary inappropriate track of the glider. South of the flow reversal in section 2, between 24°N and 23.5°N, a non-negligible along track flow also suggests that the computed geostrophic velocity may be under-estimating the actual current.

4 Discussion

4.1 thermohaline structure

A summary of the the water mass properties found inside Poseidon, in the GoM outside Poseidon, and in the Caribbean is shown in the T-S diagram of figure 11. The strict resemblance of Caribbean and Poseidon water below 25°C/24.7$kg\ m^{-3}$ suggests that mixing was weak at these depths and salt and heat were well conserved during the northward advection from the Caribbean to the Loop current and during the first months after eddy detachment. Though the salinity maximum remained centred around 23 °C/25.5$kg\ m^{-3}$, its depth decreased as the latter isotherm/isopycnal rose from 275 to 230 m between the two glider surveys (Figures 6a,e and 7a,e), consistent with buoyancy adjustment with the surrounding heavier water.

Changes in water mass properties from 25°C/24.7$kg\ m^{-3}$ up to the surface occured gradually during the preceding autumn and winter. Deepening of the mixed layer was associated with a rapid cooling of the surface water. Seasonal intensification of cold northern wind in the GoM during autumn and winter (*Zavala-Hidalgo et al.* [2014]) might account for the gradual transformation of the well stratified near-surface Caribbean summer water into the thick homogeneous layer observed within the top 170 m in spring as Poseidon detached.

The salinity inversion layer associated with warmer and stratified surface water observed on top of Poseidon during the glider mission seems to have appeared gradually as well. The Argo profile right after detachment showed that the homogeneous layer extended all the way up to the surface in April, and the inversion first appeared in the early June profile.

The simultaneous formation of a warm surface layer above a sharp and shallow thermocline suggests that both salinization and warming might be related to summertime surface restratification. The impact of increased radiative, latent, and sensible heat fluxes in the GoM during the end of spring and summer months (*Zavala-Hidalgo et al.* [2002]) can be evaluated by integrating the surface temperature evolution equation in the absence of the advection and lateral diffusion terms:

$$\partial_t T = \frac{Q_{net}}{\rho C_p H}, \tag{8}$$

where Q_{net} is the net surface heat flux defined as the sum of the sensible, latent, and radiative fluxes, C_p is the specific heat capacity (4×10^4 $J\ kg^{-1}\ K^{-1}$ for 20°C water), and H is a reference mixed layer depth (fixed to 40 m here). An average net heat flux of 72 $W\ m^{-2}$ is necessary to account for the observed surface temperature rise between April and September. *Zavala-Hidalgo et al.* [2002] computed such net surface heat fluxes using satellite measured radiation and bulk formula. Averaging these from April to September gives a mean flux of 65 $W\ m^{-2}$, consistent with our estimation.

The impact of increased summer evaporation on the salinization of Poseidon's surface layer can also be evaluated using the surface salinity evolution equation and the same zero-lateral diffusion and zero-advection hypothesis :

$$\partial_t S = \frac{S_0}{H}(E - P), \tag{9}$$

where S_0 is a reference salinity and (E-P) is the fresh water surface flux computed as the difference between evaporation and precipitation. The evaporation excess required to explain the +0.15 psu increase of the surface salinity on top of Poseidon between April and September is of 1.60 $mm\ d^{-1}$. Averaging NCEP Climate Forecast System Reanalysis values (*Saha et al.* [2010]) from April to September gives an evaporation excess of 1.96 $mm\ d^{-1}$, close to the required value for the observed salinization.

The deepening of the mixed layer and upper thermocline observed from north to south during the second glider transect also likely result from surface heat fluxes and turbulent mixing and might be linked to seasonal changes rather than a synoptic north-south asymmetry. The transect started in September and ended in mid-November. Such a deepening of the mixed layer in the GoM during autumn was observed and discussed by *Zavala-Hidalgo et al.* [2014]. During that same time lapse, they reported mixed layer deepening from 30 to 60 m, which they attributed to the occurrence of northerly winds.

The vertical upper thermohaline structure of Poseidon thus seems to be largely influenced by seasonal processes, suggesting that LCE suffer strong near-surface diabatic water transformation from their very formation and throughout their drift in the GoM.

The intensity of the thermohaline anomalies within Poseidon appeared to be larger than previously reported. The thermal anomaly that reached almost 10 ^oC between 200 and 250 m was associated with a downward deflection of the isotherms: the 20 ^oC isotherm plunged from 140 to 350 m corresponding to a 210 m dive. Previous LCE observations from *Elliott* [1982] and *Forristall et al.* [1992] reported weaker downward deflections of respectively -165 and -150 m. Poseidon's isotherm deflection however remains well below the 500 m plunging observed in some Gulf stream anticyclonic rings (*Joyce* [1984]).

The saline anomaly was also stronger and deeper than previously observed: The salinity maximum reached 36.97 psu at 275 m while *Elliott* [1982] and *Cooper et al.* [1990] respectively reported maxima of 36.69 psu at 210 m and 36.8 psu around 250 m on the 22.5 ^oC isotherm. Considering the 36.6 psu isohaline as the limit of the saline core, that of Poseidon was 140 m thick: twice thicker than observed by *Elliott* [1982].

The striking heat and salt conservation within the saline core of Poseidon months after its detachment, and the similarity of this water mass with that observed in the Caribbean one year prior to the experiment suggest that the difference between the deep salinity maximum of Poseidon and that of previously sampled LCEs might not depend on local water mass transformation or shedding season: below 200 m, the water found in the Caribbean is SUW (*Hernández-Guerra and Joyce* [2000]), part of which is formed by subduction in the subtropical and tropical North Atlantic (*Qu et al.* [2016]). The salinity maximum in the Caribbean and GoM is thus remotely controlled by preceding SSS in the subtropical North-Atlantic. The latter was shown to experience interannual and decadal variability of over 0.5 psu (*Rosenheim et al.* [2005]; *Moses et al.* [2006]), and the subduction rate of SUW can vary by a factor 2 on these time scales (*Qu et al.* [2016]). Subtrop-

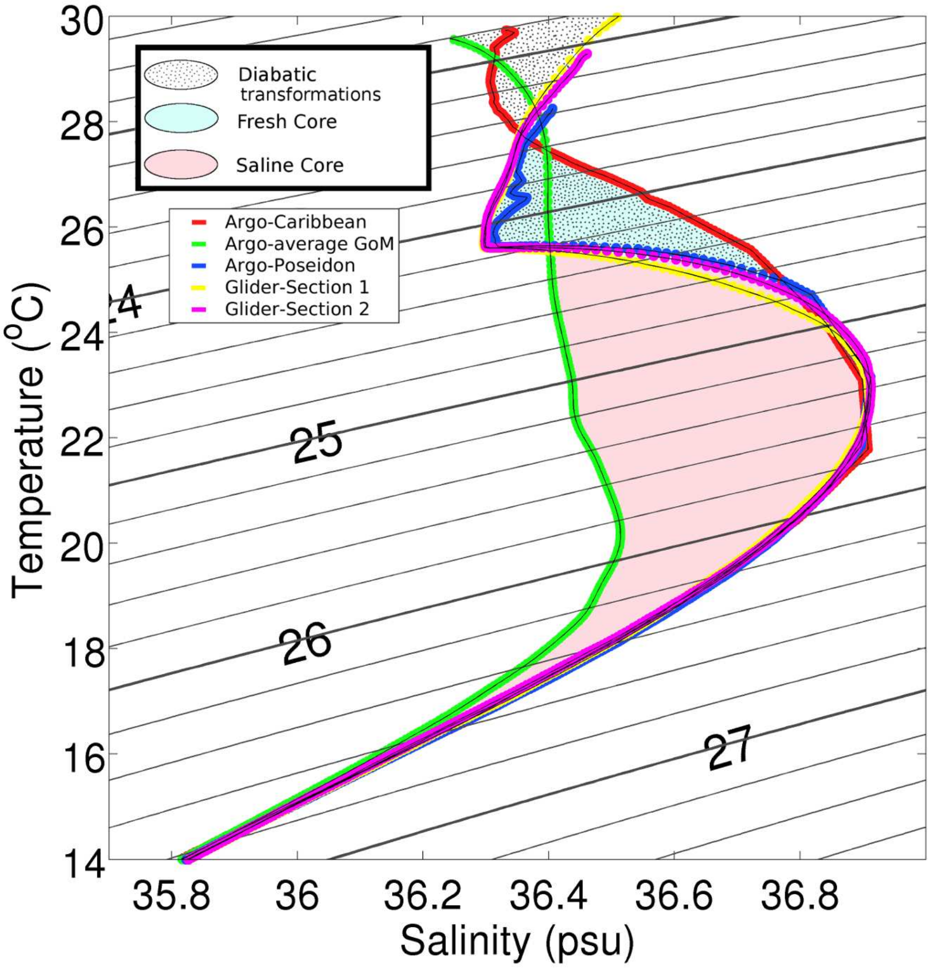

Figure 11. T-S diagram of selected profiles: northwest Caribbean Argo profile (red line), average GoM water from Argo profiles (green), recently formed Poseidon Argo profile (blue), average Poseidon profile from glider section 1 (yellow) and 3 (magenta). The light red filled area illustrates the saline core and the light blue one is the fresh core. The dotted area stands for the transformation from pure Caribbean water to Poseidon water through surface diabatic processes (Surface heat fluxes and diapycnal mixing).

ical SSS maximum, hence SUW's salinity, were shown to be closely correlated with the North Atlantic Oscillation (NAO) (*Moses et al.* [2006]; *Rosenheim et al.* [2005]; *Qu et al.* [2016]): wind anomalies associated with NAO variations largely control both evaporation and MLD, resulting in saltier (fresher) SUW during periods of positive (negative) NAO. Cross examination of Hurrell station-based NAO index (*Hurrell and Deser* [2010]) and the salinity maxima observed in past studies seems to confirm this trend of fresher LCEs during, or soon after negative NAO episodes: The moderate salinity (36.6 psu) reported by *Elliott* [1982] in 1966, 1967 and 1970 were measured during negative NAO (1966-1967), or moderately positive NAO (1970) following a strong negative year (1969); *Cooper et al.* [1990] reported a maximum salinity of 36.8 psu in 1983, as the NAO was positive, but following a 6 years negative period; a similar salinity maximum of 36.8 psu was observed by *Rudnick et al.* [2015] in 2011-2012, as the NAO switched from being negative between 2009 and 2011 to positive in 2012; the exceptionally large salinity maximum (up to 36.97) reported in the present paper was observed after 3 years of positive NAO. Some prudence is required when analysing the link between LCE's salinity maximum and NAO index, as changes in the North Atlantic subtropical salinity maximum do not impact instantly Caribbean and LC's SUW: the SUW subduction zone is located 3000 to 5000 km east of the Yucatan channel, and a lag in changes of properties is to be expected. Considering average westward currents of 10 $cm\ s^{-1}$ (*Olbers et al.* [1985]) and a distance of 4000 km (*Qu et al.* [2016]), it would take 460 days for recently subducted SUW to reach the Yucatan channel. NAO of the two previous years might thus be more relevant to explain LCE's properties than instantaneous NAO. Note also that a multidecadal trend of salinization of the subtropical North-Atlantic since the late 1980's was reported by *Gordon and Giulivi* [2008], and might also account for the increase in LCE's salinity between *Elliott* [1982]'s observations and those reported in this manuscript. A detailed study of the relationship between LCE's properties and preceding basin-scale conditions in the North Atlantic, including a precise evaluation of the typical advection time of SUW between its subduction zone and the LC would be of interests to understand LCE's interannual to decadal variability.

4.2 Heat and Salt budgets

In a study of heat budgets in the GoM, *Etter* [1983] revealed the existence of a non-negligible residual heat advection (8 $W\ m^{-2}$) from the Eastern to the western GoM which they attributed to LCEs. As the fate of LCEs is to eventually diffuse their heat and salt into the Western GoM, it is of interest to evaluate the total content they carry.

The total salt excess carried by Poseidon was of $\hat{S}_c \approx 2.2{\pm}0.1 \times 10^{10}$ tons. The heat excess was of $\hat{Q}_c \approx 9.4 \pm 0.5 \times 10^{12}\ MJ$. For comparison purpose with *Elliott* [1982]'s work, those values can be normalized by the Eddy's surface: the surface averaged heat and salt anomalies associated with Poseidon were of respectively $1{\pm}0.1 \times 10^{10}\ J\ m^{-2}$ and $242{\pm}8\ kg\ m^{-2}$: larger than *Elliott* [1982]'s estimates ($0.7 \times 10^{10}\ J\ m^{-2}$ and $170\ kg\ m^{-2}$).

In the long run, total diffusion of LCE's heat and salt toward surrounding GoM water is inevitable. Under the rough assumption that these redistribute homogeneously over the entire GoM, it is possible to assess the salinization and warming of GoM water induced by Poseidon. The GoM's volume was computed using the ETOPO1 bathymetry data base (*Amante and Eakins* [2009]). From bottom to surface, it is approximatively $2.32 \times 10^6\ km^3$. Mixing Poseidon's 23 billion tons of salt excess in this water volume would increase its salinity by $9.1 \times 10^{-3}\ psu$. The temperature increase by mixing the eddy's heat excess would be $9.4 \times 10^{-2}\ {}^oC$. Assuming heat and salt diffusion is limited vertically and the latter is confined within the top 1000 m, GoM's salinity and temperature would increase by $2.3 \times 10^{-2}\ psu$ and $2.4 \times 10^{-1}\ {}^oC$.

Under the hypothesis of one LCE released per year, and still assuming homogeneous and isotropic mixing in the top 1000 m of the GoM, the mean yearly net heat flux and fresh water input required to balance the heat gain and salt excess carried by Poseidon obey:

$$\iint_{\mathcal{A}_g} ds \int_{Jan}^{Dec} Q_{net}\, dt = \hat{Q}_c, \tag{10}$$

$$\iint_{\mathcal{A}_g} ds \int_{Jan}^{Dec} I_{fw}\, dt = \frac{1000\hat{S}_c}{\rho S_g}, \tag{11}$$

where $\mathcal{A}_g$ is the GoM's surface ($1.6 \times 10^6\ km^2$), Q_{net} is the sum of radiative, latent, sensible, and advective heat fluxes and I_{fw} is the sum of river run offs, evaporation, and precipitation. S_g is the CGW salinity averaged on the top 1000 m (found to be 35.4 psu here). The 1000 factor appears to transform psu into $kg\ kg^{-1}$.

Integrating equation 10, a yearly mean net loss of 14.89 $W\ m^{-2}$ appears necessary to balance Poseidon's heat excess and a yearly mean 1.01 $mm\ day^{-1}$ fresh water input is necessary to balance its salt excess. Annual mean net surface heat fluxes over the GoM were estimated in various studies over the past and were reviewed by *Zavala-Hidalgo et al.* [2002]. They range from -24.1 to +46.6 $W\ m^{-2}$ depending on the source. The results reported here obviously suggest that negative values are required to balance LCEs. *Elliott* [1982] estimated the fresh water flux in the Gulf of Mexico to be 349 $km^3\ year^{-1}$, corresponding to an average fresh water input of 0.6 $mm\ day^{-1}$, which would be insufficient to balance Poseidon's salt excess in a year. *Elliott* [1982] estimated that, to balance their observed fresh water input, 0.74 LCEs per year were necessary. In the case of Poseidon, only 0.59 would be sufficient.

Of course, these numbers are subject to caution. The necessary fluxes computed here rely on the assumption of one LCE detachment per year, and of Poseidon being a typical LCE. The heat fluxes found in the literature are also to be carefully interpreted as they largely differ from one another. Advective heat fluxes on the southern and northern GoM shelves are also expected to play a non negligible role in heat redistribution and were shown to be also a heat gain for the western GoM (*Chang and Oey* [2010b]), but to our knowledge, no long term observation of such boundary advective heat fluxes were published. The fresh water input data also need to be interpreted with care as they might not be exhaustive, with a notable lack of knowledge on the Yucatan subterranean fresh water discharge (Julio Sheinbaum, personal communication). Above all, they are subject to important inter-annual variability.

4.3 Velocity stucture

Geostrophic velocity in Poseidon was maximum in subsurface and on the outer edges of the thermohaline anomaly, where the density gradients reach their maximum. It was obvious in the form of a high velocity annulus, typical of vortex rings. Vertical shear was intense in the top 300 m, and reached its maximum between 100 and 200 m in the periphery of the velocity maxima. Contrary to the thermohaline properties of Poseidon, those velocities are relatively weak for a young LCE with maxima ranging from 0.8 to 1.55 $m\ s^{-1}$. Though *Indest et al.* [1989] and *Glenn and Ebbesmeyer* [1993] reported weaker maximum velocities of 0.8 to 1.2 $m\ s^{-1}$ using surface drifting buoys, most recent direct measurements with shipboard-mounted ADCP reported faster currents: *Forristall et al.* [1992] observed velocity maxima of 1.78 $m\ s^{-1}$, *Cooper et al.* [1990] and *Koch et al.* [1991] 2 $m\ s^{-1}$ and *Guan et al.* [2011] 2.75 $m\ s^{-1}$. The use of the geostrophic approximation, along with the fact that the velocity reported here are only a measure of the component normal to the glider's trajectory, likely accounts for the relative weakness of Poseidon's currents compared to previous direct measurements. The abnormally high salinity may also reduce the density anomaly, hence the pressure gradient and contribute to the relatively weak velocity maxima.

In both transects, higher velocity was found north of the eddy than south. Such an asymmetry in the velocity distribution was observed by *Forristall et al.* [1992], but contrary to the present observations, their velocities were stronger south than north. Various processes were proposed to explain this asymmetry: *Forristall et al.* [1992] suggested that ellipticity of the eddy would result in stronger density gradient along the semi-minor axes and weaker along the semi-major axes, while *Glenn and Ebbesmeyer* [1993] aimed that mixed planetary-topographic Rossby waves dispersions would increase the gradients in front of the drifting eddy and decrease them past it. Though these processes may have an impact on previously reported asymmetry, they hardly explain our observations: Rossby waves are expected to increase gradients southwest of a southwestward drifting eddy while here, the maximum velocity appeared to be larger on the northern edge. The maximum velocity was observed at the end of section 1 as Poseidon was almost circular, and the weaker ones at the southern end of section 2, along the semi-minor axes of the ellipse where the strongest density gradient would be expected from *Forristall et al.* [1992]'s theory. It is important to note that neighbouring structures such as mesoscale or submesoscales eddies or filaments can significantly modify the surrounding thermohaline patterns hence modify the density gradients. Most of these structures have strong velocity, and spacial scales under the altimetry's coarse resolution, which makes them difficult to clearly identify.

Note also that the geostrophic velocity presented here are subject to caution. One of the major concerns when sampling rapidly drifting eddies with a slow vehicle is obviously the synopticity, whose lack can affect any physical quantity relying on gradients. The distance used to compute the density gradients is the distance traveled by the glider. In theory, a synoptic representation of the gradient of any tracer χ carried by an eddy must be computed in a spatial referential translating at the same speed as the eddy. In the simple case of the eddy and glider trajectories being on the same straight line, the relationship between the synoptic tracer gradient in the eddy referential and the tracer gradient measured by the glider reads:

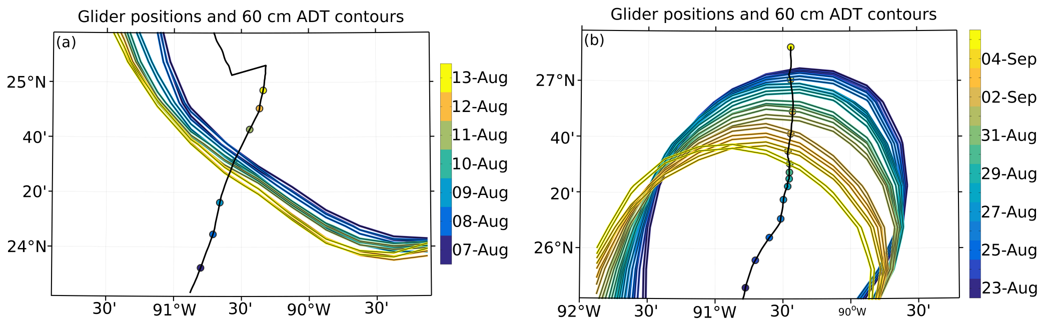

Figure 12. Illustration of the synopticity variations during the glider survey. a (b): Daily position of the 0.6 m ADT isopleth (contours) and the simultaneous position of the glider (dots) during the crossing of the southern (northern) velocity maximum of section 1. Time is colour-coded. During the southern crossing, the frontal edge of the eddy was almost stationary, while it was drifting fast towards the approaching glider. The southern velocity maximum was thus measured with a better synopticity than the northern.

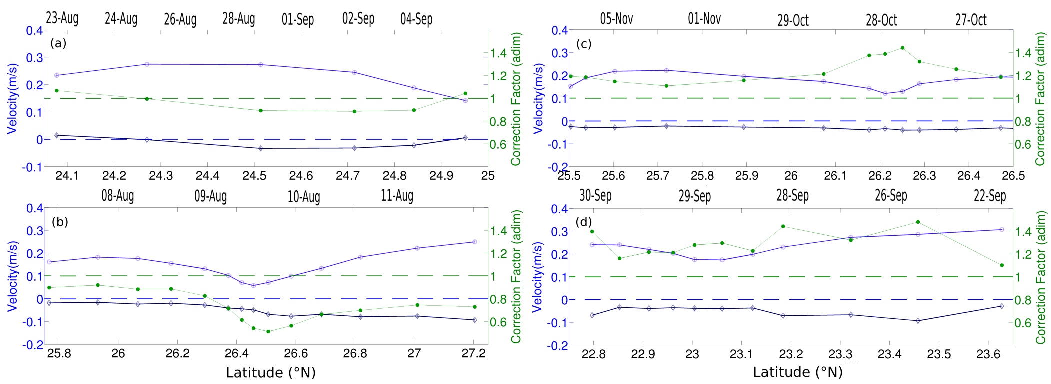

Figure 13. Evolution of the correction factor described in equation 13 for the southern and northern edges of sections 1 and 2 (green lines and dots). The glider and front velocity are represented as light and dark blue lines, respectively. a: Section 1 north; b: Section1 south; c: section 2 south, d: section 2 north.

$$\left.\frac{\partial \chi}{\partial x}\right|_e = \frac{U_g}{U_g - U_e} \left.\frac{\partial \chi}{\partial x}\right|_f, \tag{12}$$

where U_g is the glider's velocity, U_e is the eddy drift speed, and $\frac{\partial \chi}{\partial x}|_e$ and $\frac{\partial \chi}{\partial \chi}|_f$ are the tracer gradients in the eddy and in the fixed referential, respectively. The singular case $U_g = U_e$ where the glider travels at the same velocity as the eddy is compensated by a zero-gradient on the right hand side (the glider keeps on sampling the exact same water mass). As shown in figure 3, Poseidon's drift speed exhibited quite large variability during the glider survey, so that the error on geostrophic velocity also varies along each section. This is particularly obvious when examining the displacements of the eddy as the glider crossed the velocity maxima north and south of section 1 (figure 12). While the eddy was almost stationary during the southern crossing, assuring a good level of synopticity of the glider's observations, it was drifting fast in the opposite direction of the glider's motion during the northern crossing, suggesting an overestimation of the geostrophic velocity.

To evaluate the magnitude of the error on geostrophic velocity, a correction factor was derived from equation 12:

$$C_f = \frac{U_g}{U_g - U_e}. \tag{13}$$

U_e is computed using ADT data. To take into account the effect of the deformation of the eddy along with its drift, rather than considering the drift of the centre of the eddy alone, U_e is defined as the velocity of the fronts associated with the velocity maxima. It is computed considering the displacements of the intersection between the glider trajectory and the closest ADT contour between two consecutively available ADT maps. Figure 13 shows the evolution of the glider velocity (light blue line and dots), the front velocity (dark blue), and the associated correction factor (green), during the crossing of the southern and northern velocity maxima of sections 1 and 2. During section 1, the glider was moving against the eddy drift while suring section 2, it was moving in the same direction. This results in correction factors smaller than unity for section 1, and greater for section 2. The fast drift of the eddy during the northern crossing of section 1 results in a correction factor reaching 0.5 between 28 August and 01 September, and remaining below 0.7 until the end of the section. On the other hand, it remains between 0.9 and 1 during the southern crossing of section 1. This likely explains part of the north-south assymetry in the geostrophic velocity section. During section 3, the correction factor also eventually reached large values (upto 1.45), as the glider's velocity decreased and the latter hardly "chased" the eddy between 27 and 29 October. It remains also between 1.3 and 1.45 as the glider crossed the southern velocity maximum of section 3 between 25 and 28 September, which might also explain part of the north-south asymetry

Unfortunately, ADT maps have coarse spatial and temporal resolutions: the data used are daily composites built from the 5 previous and next days. Hence, the correction factor represents an approximative measure of the error, rather than an effective coefficient that could be used to correct the velocity sections shown in figure 10.

This effect could be largely responsible for the higher velocity measured during the first transect when the glider and the eddy moved in opposite directions than during the second transect when they moved in the same direction. The important variability of the eddy drift speed could result in locally stronger errors, but it is believed that the use of a large de-correlation scale, as well as the fact that the glider trajectory makes a non-negligible angle with the eddy drift direction tend to smooth out the error.

5 Summary and conclusion

The vertical structure of LCE Poseidon was revealed during the two glider transects. Several opportunity Argo float profiles helped to understand the origin and the transformation processes of the water mass found in the eddy, while the altimetry data allowed the description of the temporal evolution of Poseidon as well as its history previous to the glider mission. A combined analysis of the latter data provided a better understanding of the vertical structure of LCEs and the processes leading to it. The main conclusions of this work can be summed-up as follows :

- Poseidon's thermal structure consisted of a nearly $10°C$ warm anomaly between 200 and 250 m; larger than previous observations.
- Salinity was distributed following a double core pattern: One subsurface fresh core and one deeper saline core.
- The salinity maximum was larger than LCE's typical values, reaching 36.97 psu.
- It was well conserved during its journey from the Yucatan Basin toward the LC and after more than 6 months of eddy drift.

- The fresh core formed by intense surface mixing during the winter preceding Poseidon's detachment.
- The eddy was characterized by a body of extremely weakly stratified water embedded in a stratified watermass. It was isolated from the surface by summertime stratification linked to positive heat fluxes and intense evaporation.
- The heat and salt excess carried by Poseidon would take more than a year to be balanced by typical GoM's surface heat flux and fresh water input.
- Intense geostrophic velocity maxima were found in subsurface, near the edge of the thermohaline core, and were weaker than most recently observed LCEs.

Though these results reveal in details the structure of Poseidon, they also suggest that LCE structure might differ significantly from one another because of the importance of surface processes in determining the thermohaline properties of the top 200 m. Interannual variability of the SUW also implies a variability in the saline core properties below 200 m. Poseidon's structure results from a combination of particular atmospheric and oceanographic conditions, and more LCEs must be surveyed to assess a true understanding of their typical structures, dynamics, and impacts. Of particular interest is the study of the long term evolution and dissipation of LCEs. Repeated surveys of LCEs over their entire life cycle will help to understand the mixing processes leading to the release of heat and salt toward the GoM and the formation of the CGW. Combining a better knowledge of LCEs diffusion and dissipation, and of the link between their thermohaline structure and large scale inter-annual processes (such as NAO), could help to assess the interannual to decadal response of the GoM in the context of a changing climate.

Acknowledgments

The glider mission was performed by the Grupo de Monitoreo Oceanografo con Gliders (CICESE, UNAM, CIDESI, CICATA) and is part of the Gulf of Mexico Research Consortium (CIGOM) project funded by CONACYT. T. Meunier was funded by a postdoctoral scholarship from CICESE, funded via a grant of the National Council of Science and Technology of Mexico - Secretariat of Energy -Hidrocarbons Trust, project 201441. Argo data were collected and made freely available by the International Argo Program and the national programs that contribute to it (http://www.argo.ucsd.edu, http://argo.jcommops.org, http://www.coriolis.eu.org/Observing-the-Ocean/ARGO). The Argo Program is part of the

Global Ocean Observing System. The altimeter products were produced by Ssalto/Duacs and distributed by Aviso, with support from Cnes (http://www.aviso.altimetry.fr/duacs/).

The authors are grateful to Pr. Des Barton, Pr. Julio Sheinbaum, Pr. Paula Perez Brunius, Dr. Orens Pasqueron de Fommervaut, Dr. Pierre Damien and Dr. Joao Marcos Azevedo Correia De Souza for the valuable discussions and suggestions before and during the glider surveys and during the elaboration of this manuscript.

T. Meunier would like to dedicate this paper to the memory of Jean-Pierre Bergeron, who devoted his life to the understanding of the Ocean.

The raw data set used in this study can be visualized on the GMOG's webpage: https://gliders.cicese.mx/. The full data can be distributed on demand on the same web page.

Table A.1. List of Argo float profiles used to identify Poseidon's water mass origin from the northwest Caribbean to the tip of the LC (a) and to compute the GoM water mass properties outside Poseidon (b)

Float serial number	Cycle number	Date	Longitude (°E)	Latitude (°N)	Purpose of the profile
4901061	191	22 Sep 2015	-84.097	19.884	(a)
4901061	195	01 Nov 2015	-85.425	20.283	—
4901061	203	20 Jan 2016	-85.641	22.056	—
4901061	207	29 Fev 2016	-87.099	23.951	—
4901061	212	19 Apr 2016	-86.332	26.502	—
4901061	217	08 Jun 2016	-86.803	25.589	—
4901061	219	28 Jun 2016	-86.467	25.890	(b)
4901061	220	08 Jul 2016	-85.547	25.123	—
4901061	221	18 Jul 2016	-85.141	25.813	—
4901061	222	28 Jul 2016	-86.122	26.269	—
4901061	223	07 Aug 2016	-87.037	26.564	—
4901061	224	17 Aug 2016	-86.663	26.675	—
4901643	188	12 May 2016	-91.321	24.131	—
4901643	189	16 May 2016	-91.363	24.226	—
4901643	190	20 May 2016	-91.458	24.368	—
4901643	191	24 May 2016	-91.592	24.467	—
4901643	192	28 May 2016	-91.793	24.570	—
4901643	193	01 Jun 2016	-92.069	24.670	—
4901643	194	05 Jun 2016	-92.342	24.633	—
4901643	195	09 Jun 2016	-92.633	24.620	—
4901643	196	13 Jun 2016	-92.759	24.668	—
4901643	197	17 Jun 2016	-92.973	24.756	—
4901643	198	21 Jun 2016	-93.064	24.841	—
4901643	299	25 Jun 2016	-93.347	24.882	—
4901643	200	29 Jun 2016	-93.481	24.975	—
4901643	201	03 Jul 2016	-93.616	25.042	—
4901643	202	07 Jul 2016	-93.724	25.132	—
4901643	203	11 Jul 2016	-93.760	25.186	—
4901643	204	15 Jul 2016	-93.613	25.199	—
4901643	205	19 Jul 2016	-93.500	25.165	—
4901643	206	23 Jul 2016	-93.420	25.091	—
4901643	207	27 Jul 2016	-93.343	24.996	—
4901643	208	31 Jul 2016	-93.258	24.961	—
4901643	209	04 Aug 2016	-93.186	24.827	—
4901643	210	08 Aug 2016	-93.179	24.735	—
4901643	211	12 Aug 2016	-93.233	24.547	—
4901643	212	16 Aug 2016	-93.311	24.415	—
4901643	213	20 Aug 2016	-93.407	24.294	—
4901643	214	24 Aug 2016	-93.404	24.218	—
4901643	215	28 Aug 2016	-93.510	24.155	—
4901643	216	01 Sep 2016	-93.700	24.122	—
4901643	217	05 Sep 2016	-93.880	24.067	—
4901643	218	09 Sep 2016	-94.184	24.070	—
4901643	219	13 Sep 2016	-94.596	24.180	—
4901643	220	17 Sep 2016	-94.949	24.339	—

A: Appendix: List of Argo profiles

References

Amante, C., and B. W. Eakins (2009), *ETOPO1 1 arc-minute global relief model: procedures, data sources and analysis*, US Department of Commerce, National Oceanic and Atmospheric Administration, National Environmental Satellite, Data, and Information Service, National Geophysical Data Center, Marine Geology and Geophysics Division Colorado.

Armi, L., D. Hebert, N. Oakey, J. F. Price, P. L. Richardson, H. Thomas Rossby, and B. Ruddick (1989), Two Years in the Life of a Mediterranean Salt Lens, *Journal of Physical Oceanography*, *19*, 354–370, doi:10.1175/1520-0485(1989)019<0354:TYITLO>2.0.CO;2.

Austin, G. B. (1955), Some recent oceanographic surveys of the gulf of mexico, *Eos, Transactions American Geophysical Union*, *36*(5), 885–892.

Barnes, S. L. (1964), A Technique for Maximizing Details in Numerical Weather Map Analysis., *Journal of Applied Meteorology*, *3*, 396–409, doi:10.1175/1520-0450(1964)003<0396:ATFMDI>2.0.CO;2.

Barnes, S. L. (1994), Applications of the Barnes Objective Analysis Scheme. Part I: Effects of Undersampling, Wave Position, and Station Randomness, *Journal of Atmospheric and Oceanic Technology*, *11*, 1433, doi:10.1175/1520-0426(1994)011<1433:AOTBOA>2.0.CO;2.

Biggs, D. C. (1992), Nutrients, plankton, and productivity in a warm-core ring in the western Gulf of Mexico, , *97*, 2143–2154, doi:10.1029/90JC02020.

Biggs, D. C., and F. E. Müller-Karger (1994), Ship and satellite observations of chlorophyll stocks in interacting cyclone-anticyclone eddy pairs in the western Gulf of Mexico, , *99*, 7371–7384, doi:10.1029/93JC02153.

Biggs, D. C., G. S. Fargion, P. Hamilton, and R. R. Leben (1996), Cleavage of a Gulf of Mexico Loop Current eddy by a deep water cyclone, , *101*, 20,629–20,642, doi:10.1029/96JC01078.

Chang, Y.-L., and L.-Y. Oey (2010a), Why Can Wind Delay the Shedding of Loop Current Eddies?, *Journal of Physical Oceanography*, *40*, 2481–2495, doi:10.1175/2010JPO4460.1.

Chang, Y.-L., and L.-Y. Oey (2010b), Eddy and Wind-Forced Heat Transports in the Gulf of Mexico, *Journal of Physical Oceanography*, *40*, 2728–2742, doi:10.1175/2010JPO4474.1.

Cooper, C., G. Z. Forristall, and T. M. Joyce (1990), Velocity and hydrographic structure of two Gulf of Mexico warm-core rings, , *95*, 1663–1679, doi: 10.1029/JC095iC02p01663.

Cushman-Roisin, B., B. Tang, and E. P. Chassignet (1990), Westward Motion of Mesoscale Eddies, *Journal of Physical Oceanography*, *20*, 758–768, doi:10.1175/1520-0485(1990)020<0758:WMOME>2.0.CO;2.

Domingues, R., G. Goni, F. Bringas, B. Muhling, D. Lindo-Atichati, and J. Walter (2016), Variability of preferred environmental conditions for atlantic bluefin tuna (thunnus thynnus) larvae in the gulf of mexico during 1993–2011, *Fisheries Oceanography*, *25*(3), 320–336.

Elliott, B. A. (1982), Anticyclonic Rings in the Gulf of Mexico, *Journal of Physical Oceanography*, *12*, 1292–1309, doi:10.1175/1520-0485(1982)012<1292:ARITGO>2.0.CO;2.

Eriksen, C. C., T. J. Osse, R. D. Light, T. Wen, T. W. Lehman, P. L. Sabin, J. W. Ballard, and A. M. Chiodi (2001), Seaglider: A long-range autonomous underwater vehicle for oceanographic research, *IEEE Journal of oceanic Engineering*, *26*(4), 424–436.

Etter, P. C. (1983), Heat and Freshwater Budgets of the Gulf of Mexico, *Journal of Physical Oceanography*, *13*, 2058–2069, doi:10.1175/1520-0485(1983)013<2058:HAFBOT>2.0.CO;2.

Forristall, G. Z., K. J. Schaudt, and C. K. Cooper (1992), Evolution and kinematics of a loop current eddy in the Gulf of Mexico during 1985, , *97*, 2173–2184, doi: 10.1029/91JC02905.

Garau, B., S. Ruiz, W. G. Zhang, A. Pascual, E. Heslop, J. Kerfoot, and J. Tintoré (2011), Thermal Lag Correction on Slocum CTD Glider Data, *Journal of Atmospheric and Oceanic Technology*, *28*, 1065–1071, doi:10.1175/JTECH-D-10-05030.1.

Glenn, S. M., and C. C. Ebbesmeyer (1993), Drifting buoy observations of a loop current anticyclonic eddy, , *98*, 20, doi:10.1029/93JC02078.

Goni, G. J., J. A. Trinanes, A. MacFadyen, D. Streett, M. J. Olascoaga, M. L. Imhoff, F. Muller-Karger, and M. A. Roffer (2015), Variability of the deepwater horizon surface oil spill extent and its relationship to varying ocean currents and extreme weather conditions, in *Mathematical modelling and numerical simulation of oil pollution problems*, pp. 1–22, Springer.

Gordon, A. L., and C. F. Giulivi (2008), Sea surface salinity trends: over fifty years within the subtropical north atlantic, *Oceanography*, *21*(1), 20–29.

Guan, X. A., A. Brown, A. Brown, et al. (2011), On the eddy structure in the northern gulf of mexico-implications of vmadcp observations from 2005 to 2007, in *Offshore Technology Conference*, Offshore Technology Conference.

Hamilton, P., G. S. Fargion, and D. C. Biggs (1999), Loop Current Eddy Paths in the Western Gulf of Mexico, *Journal of Physical Oceanography*, *29*, 1180–1207, doi: 10.1175/1520-0485(1999)029<1180:LCEPIT>2.0.CO;2.

Hernández-Guerra, A., and T. M. Joyce (2000), Water masses and circulation in the surface layers of the Caribbean at 66deg$W,,27,$3497 $-$ $-$3500,doi : 10.1029/1999GL011230.

Hoteit, I., T. Hoar, G. Gopalakrishnan, N. Collins, J. Anderson, B. Cornuelle, A. Köhl, and P. Heimbach (2013), A MITgcm/DART ensemble analysis and prediction system with application to the Gulf of Mexico, *Dynamics of Atmospheres and Oceans*, *63*, 1–23, doi:10.1016/j.dynatmoce.2013.03.002.

Hurrell, J. W., and C. Deser (2010), North Atlantic climate variability: The role of the North Atlantic Oscillation, *Journal of Marine Systems*, *79*, 231–244, doi: 10.1016/j.jmarsys.2009.11.002.

Ichiye, T. (1959), Circulation and water-mass distribution in the gulf of mexico, *Journal of Geophysical Research*, *64*(8), 1109–1110.

Indest, A., A. Kirwan, J. Lewis, and P. Reinersman (1989), A synopsis of mesoscale eddies in the gulf of mexico, *Elsevier oceanography series*, *50*, 485–500.

Joyce, T. M. (1984), Velocity and Hydrographic Structure of a Gulf Stream Warm-Core Ring, *Journal of Physical Oceanography*, *14*, 936–947, doi:10.1175/1520-0485(1984)014<0936:VAHSOA>2.0.CO;2.

Koch, S., J. Barker, J. Vermersch, et al. (1991), The gulf of mexico loop current and deep-water drilling, *Journal of Petroleum Technology*, *43*(09), 1–046.

Le HéNaff, M., V. H. Kourafalou, Y. Morel, and A. Srinivasan (2012), Simulating the dynamics and intensification of cyclonic Loop Current Frontal Eddies in the Gulf of Mexico, *Journal of Geophysical Research (Oceans)*, *117*, C02034, doi: 10.1029/2011JC007279.

Leben, R. R. (2005), Altimeter-derived loop current metrics, *Washington DC American Geophysical Union Geophysical Monograph Series*, *161*, 181–201, doi:

10.1029/161GM15.

Leipper, D. F. (1970), A sequence of current patterns in the Gulf of Mexico, , *75*, 637–657, doi:10.1029/JC075i003p00637.

Lipphardt, B., A. Poje, A. Kirwan, L. Kantha, and M. Zweng (2008), Death of three loop current rings, *Journal of Marine Research*, *66*(1), 25–60.

Lueck, R. G. (1990), Thermal Inertia of Conductivity Cells: Theory, *Journal of Atmospheric and Oceanic Technology*, *7*, 741–755, doi:10.1175/1520-0426(1990)007<0741:TIOCCT>2.0.CO;2.

Lueck, R. G., and J. J. Picklo (1990), Thermal Inertia of Conductivity Cells: Observations with a Sea-Bird Cell, *Journal of Atmospheric and Oceanic Technology*, *7*, 756–768, doi:10.1175/1520-0426(1990)007<0756:TIOCCO>2.0.CO;2.

Lugo-Fernández, A., and R. R. Leben (2010), On the Linear Relationship between Loop Current Retreat Latitude and Eddy Separation Period, *Journal of Physical Oceanography*, *40*, 2778–2784, doi:10.1175/2010JPO4354.1.

Molina, M., R. Timmer, and J. Allen (2016), Importance of the gulf of mexico as a climate driver for us severe thunderstorm activity, *Geophysical Research Letters*, *43*(23).

Moses, C. S., P. K. Swart, and B. E. Rosenheim (2006), Evidence of multidecadal salinity variability in the eastern tropical North Atlantic, *Paleoceanography*, *21*, PA3010, doi:10.1029/2005PA001257.

Nof, D. (1981), On the β-Induced Movement of Isolated Baroclinic Eddies, *Journal of Physical Oceanography*, *11*, 1662–1672, doi:10.1175/1520-0485(1981)011<1662:OTIMOI>2.0.CO;2.

O'Connor, B. M., R. A. Fine, and D. B. Olson (2005), A global comparison of subtropical underwater formation rates, *Deep Sea Research Part I: Oceanographic Research*, *52*, 1569–1590, doi:10.1016/j.dsr.2005.01.011.

Oey, L.-Y., T. Ezer, G. Forristall, C. Cooper, S. DiMarco, and S. Fan (2005), An exercise in forecasting loop current and eddy frontal positions in the Gulf of Mexico, , *32*, L12611, doi:10.1029/2005GL023253.

Olbers, D. J., M. Wenzel, and J. Willebrand (1985), The Inference of North Atlantic Circulation Patterns From Climatological Hydrographic Data, *Reviews of Geophysics*, *23*, 313, doi:10.1029/RG023i004p00313.

Pietri, A., V. Echevin, P. Testor, A. Chaigneau, L. Mortier, C. Grados, and A. Albert (2014), Impact of a coastal-trapped wave on the near-coastal circulation of the Peru upwelling system from glider data, *Journal of Geophysical Research (Oceans)*, *119*, 2109–2120, doi:10.1002/2013JC009270.

Qu, T., L. Zhang, and N. Schneider (2016), North Atlantic Subtropical Underwater and Its Year-to-Year Variability in Annual Subduction Rate during the Argo Period, *Journal of Physical Oceanography*, *46*, 1901–1916, doi:10.1175/JPO-D-15-0246.1.

Rosenheim, B. E., P. K. Swart, S. R. Thorrold, A. Eisenhauer, and P. Willenz (2005), Salinity change in the subtropical Atlantic: Secular increase and teleconnections to the North Atlantic Oscillation, , *32*, L02603, doi:10.1029/2004GL021499.

Rudnick, D. L., and S. T. Cole (2011), On sampling the ocean using underwater gliders, *Journal of Geophysical Research (Oceans)*, *116*, C08010, doi:10.1029/2010JC006849.

Rudnick, D. L., R. E. Davis, C. C. Eriksen, D. M. Fratantoni, and M. J. Perry (2004), Underwater gliders for ocean research, *Marine Technology Society Journal*, *38*(2), 73–84.

Rudnick, D. L., G. Gopalakrishnan, and B. D. Cornuelle (2015), Cyclonic Eddies in the Gulf of Mexico: Observations by Underwater Gliders and Simulations by Numerical Model, *Journal of Physical Oceanography*, *45*, 313–326, doi:10.1175/JPO-D-14-0138.1.

Ruiz, S., A. Pascual, B. Garau, Y. Faugère, A. Alvarez, and J. Tintoré (2009), Mesoscale dynamics of the Balearic Front, integrating glider, ship and satellite data, *Journal of Marine Systems*, *78*, S3–S16, doi:10.1016/j.jmarsys.2009.01.007.

Saha, S., S. Moorthi, H.-L. Pan, X. Wu, J. Wang, S. Nadiga, P. Tripp, R. Kistler, J. Woollen, D. Behringer, et al. (2010), The ncep climate forecast system reanalysis, *Bulletin of the American Meteorological Society*, *91*(8), 1015–1057.

Schmitz, W. J., Jr. (2005), Cyclones and westward propagation in the shedding of anticyclonic rings from the loop current, *Washington DC American Geophysical Union Geophysical Monograph Series*, *161*, 241–261, doi:10.1029/161GM18.

Shay, L. K., G. J. Goni, and P. G. Black (2000), Effects of a Warm Oceanic Feature on Hurricane Opal, *Monthly Weather Review*, *128*, 1366, doi:10.1175/1520-0493(2000)128<1366:EOAWOF>2.0.CO;2.

Thomson, R. E., and I. V. Fine (2003), Estimating Mixed Layer Depth from Oceanic Profile Data, *Journal of Atmospheric and Oceanic Technology*, *20*, 319, doi:10.1175/1520-0426(2003)020<0319:EMLDFO>2.0.CO;2.

Vukovich, F. M. (1995), An updated evaluation of the Loop Current's eddy-shedding frequency, , *100*, 8655–8659, doi:10.1029/95JC00141.

Wüst, G. (1964), *Stratification and circulation in the Antillean-Caribbean basins*, vol. 1, Columbia University Press.

Yablonsky, R. M., and I. Ginis (2013), Impact of a Warm Ocean Eddy's Circulation on Hurricane-Induced Sea Surface Cooling with Implications for Hurricane Intensity, *Monthly Weather Review*, *141*, 997–1021, doi:10.1175/MWR-D-12-00248.1.

Zavala-Hidalgo, J., A. PARÉS-SIERRA, and J. Ochoa (2002), Seasonal variability of the temperature and heat fluxes in the gulf of mexico, *Atmósfera*, *15*(2), 81–104.

Zavala-Hidalgo, J., R. Romero-Centeno, A. Mateos-Jasso, S. L. Morey, and B. Martínez-López (2014), The response of the gulf of mexico to wind and heat flux forcing: What has been learned in recent years?, *Atmósfera*, *27*(3), 317–334.